applied sciences

MDPI

Article

Research on Snow Load Characteristics on a Complex Long-Span Roof Based on Snow–Wind Tunnel Tests

Guolong Zhang [1,2], Qingwen Zhang [1,2,*], Feng Fan [1,2] and Shizhao Shen [1,2]

[1] Key Laboratory of Structures Dynamic Behavior and Control of China Ministry of Education, Harbin Institute of Technology, Harbin 150090, China; zhanggl_hit@126.com (G.Z.); fanf@hit.edu.cn (F.F.); szshen@hit.edu.cn (S.S.)

[2] Key Laboratory of Smart Prevention and Mitigation of Civil Engineering Disasters of the Ministry of Industry and Information Technology, Harbin Institute of Technology, Harbin 150090, China

* Correspondence: zhangqw@hit.edu.cn; Tel.: +86-1504-581-1536

Received: 2 September 2019; Accepted: 14 October 2019; Published: 16 October 2019

check for updates

Featured Application: This study provides a simplified method that can be applied to help preliminarily estimate the snow load on a complex roof by combining the snow loads on several simple roofs, which have been provided in the load code or obtained by numerical studies.

Abstract: A considerable number of studies have been carried out for predicting snowdrifts on roofs over the years. However, few studies have focused on snowdrifts on complex long-span roofs, as the complex shape and fine structure pose significant challenges. In this study, to simplify the calculation requirements of snow load on such roofs, work was conducted to decompose the snowdrift on a complex roof into snowdrifts on several simple roofs. First, the snow–wind tunnel test similarity criteria were investigated based on a combined air–snow–wind experimental system. Thereafter, with reference to the validated experimental similarity criteria, a series of snow–wind tunnel tests were performed for snowdrifts on a complex long-span structure under the conditions of different inflow directions. Finally, based on empirical orthogonal function (EOF) analysis, the snowdrifts on the complex roof were decomposed into basic characteristic distribution modes, including snowdrifts caused by the local and overall roof forms. The snow distribution under a specific inflow direction could be derived from the weighted combination of the basic characteristic modes, based on the wind direction coefficients. Therefore, it is possible for the snow load on a complex roof to be estimated preliminarily based on the snow distributions on several simple roofs.

Keywords: snow load; complex roof; snowdrift; EOF analysis; characteristics decomposition

1. Introduction

Snow-induced building collapse occurs frequently in long-span structures; for example, the collapse of the Katowice Trade Hall (Poland, 2006), the collapse of an ice rink in Bad Reichenhall (Germany, 2006), and the collapse of the Minnesota Vikings membrane stadium (USA, 2010). The sudden increase in the snowfall and unbalanced snow distribution, which leads to an excessive snow load in a local area, are the main reasons for such collapses [1]. Unfortunately, the snow load requirements are only provided for the design of buildings with certain simple roofs (e.g., flat roof, pitch roof, and gable roof, among others) in different national load codes [2,3], and few requirements are available for long-span structures. It is usually suggested that the snow load distribution coefficients for large or special-shaped buildings be defined following specific research or experiments in certain national codes [4,5].

In terms of the related special research methods, the computational fluid dynamics (CFD) method and wind tunnel experiment are usually adopted for the practical design of snowdrifts on or around buildings [6,7]. In the field of CFD research, Tominaga et al. [6] analyzed the snowdrift around an actual apartment building based on the revised k-ε model. In this study, the transport equation of snow concentration was solved only for snow particles suspended in the air. Thiis et al. [8,9] predicted the snow distribution on the curved roof of a sports hall under specific weather conditions. Generally, the overall snowdrift pattern fitted the measured result well and the location of end effects was reproduced close to the side edge of the roof. Beyers et al. [10] simulated the snowdrift development around a group of surface-mounted buildings and elevated structures, respectively. The analysis assisted the conceptual building design process to manage potential snowdrifts on and around these structures. The application of the CFD technique to snowdrift problems can provide detailed information on the relevant flow and phase variables in the entire calculation domain under well-controlled conditions and at a low cost. Unfortunately, the numerical technique is mainly applied to the snowdrift on small-scale roofs with usual shapes or simplified long-span roofs, as the large scale and fine structural details of complex roofs require higher resolution and higher quality grids. Cases with finer grids would be more time consuming, and the accuracy will be reduced if the grid quality is poor. Therefore, rare work was carried out on the snowdrift on complex long-span roofs by using the CFD method.

In the field of experimental research, Isyumov et al. [11] examined snowdrift formation on the lower level of a large-area two-level roof in different-surface shear stress and terrain roughness conditions. Delpech et al. [12] explored the hazard and alleviating measures of the snowdrift around the Concordia Antarctic research station by using real snow particles in the Jules Verne climatic wind tunnel. Flaga et al. [13] performed a series of snow load tests for three different complex roofs of sports facilities. Snow precipitation and wind-induced redistribution were simulated by using powdered polystyrene foam as artificial snow. The results of snow load distributions were presented for the practical structural design. Compared with the CFD method, this experiment can reproduce the snowdrift mechanism to the greatest extent and restore every detail of the building. Unfortunately, the required equipment is not always available and is usually expensive for experimental preparation and model creation. Therefore, it greatly limits the large-scale application of the experimental method in the study of snowdrift problems.

In order to analyze and summarize the snow load information on complex long-span roofs more efficiently and systematically, assisting the design process of the structure of a building, it is necessary to combine the advantages of CFD and experiment methods and avoid their limitations. Specifically, the distribution of snow load on a complex long-span roof should be analyzed in detail by using experiments. Based on the results, the distribution characteristics could be summarized systematically, before helping reduce the computing requirements for the snowdrifts on complex roofs and the large-scale analytical studies by using the CFD method. As a preliminary step, it is important to make clear the snow distribution characteristics on a complex long-span roof.

In order to express the distribution characteristics in detail, this study firstly presents the validation of the similarity criterion to figure out the experimental theory, based on an air–snow–wind combined experimental system. Thereafter, based on the similarity criterion, a description of the wind-induced snow drifting on a long-span structure with a membrane roof under different wind direction conditions is provided. Finally, according to the experimental results, the snowdrifts' characteristics on the complex membrane roof are analyzed. Three basic characteristic distribution modes and wind direction series are decomposed and derived from the results. The distribution pattern and wind direction coefficients of each mode are investigated with reference to the roof form.

2. Validation of Experimental Approach

2.1. Experimental Facility

Experimental works were carried out based on an air–snow–wind combined experimental system, which allows for the appropriate creation of natural wind velocity and turbulence profiles, as well as the precipitation environment. The snow–wind tunnel facility used belongs to the Key Laboratory of Structures Dynamic Behavior and Control of China Ministry of Education, Harbin Institute of Technology, Harbin, China, as shown in Figure 1. The facility was improved on the basis of previous research [14]. The snow–wind tunnel test chamber was closed, and the dimensions were 10 × 4.5 × 3 m. The temperature inside the chamber was the same as the outdoor air temperature, which ranged from −30 °C to −10 °C during winter. The wind velocity was measured with a hot-wire anemometer.

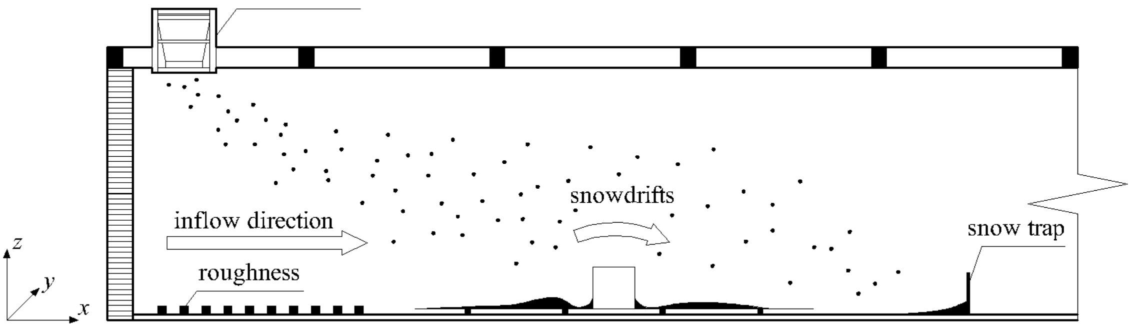

Figure 1. Schematic view of the experimental facility.

Artificial snow particles were used to simulate the snowdrift environment to deal with the combined wind–snow engineering problems (Figure 2a). The artificial snow particles were generated by spraying water droplets into freezing air with a snowmaker. A particle feeder was fixed at the top of the chamber to simulate precipitation. The snow particle feeder (Figure 2b) consisted of a stable steel frame and vibrating sieve with a perforated bottom (bottom size: 4.5 m long, 0.4 m wide; hole diameter: 5 mm). The sieve was moved by a motor with continuous speed regulation. The snowdrift flux profile was measured with a snow particle counter [15].

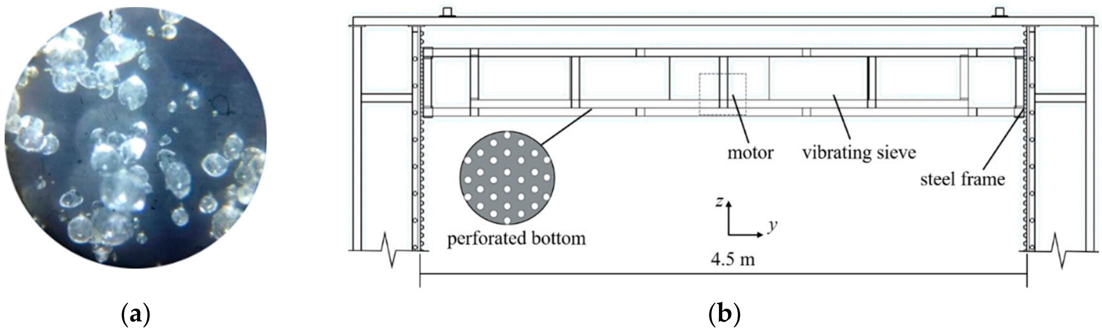

Figure 2. Snowfall simulator: (**a**) artificial snow particles; (**b**) snow particle feeder.

2.2. Similarity Criterion

The snowdrift phenomenon can be explained as solid particle transport. Depending on whether the friction velocity reaches a threshold, three particle transport mechanisms can be observed: creep, saltation, and suspension. Creep is a phenomenon in which snow particles move by rolling, sliding, or creeping at the surface; saltation is a process in which snow particles move with repeated leaping up or jumping and colliding with a snow surface; and at a higher wind velocity, particles are transported upwards by turbulent eddies and transported far downwind. Among the mechanisms, saltation has been identified as the major particle transport process, which causes approximately 67% of the total drifting mass [12]. For reliable modeling of these transport mechanisms, a reasonable similarity criterion is necessary for reduced-scale experiments. As the similarity criterions are incompatible with one another, compromises have to be made according to their relevance [12,16]. Even so, none of the models cited in the literature are able to provide a satisfying interpretation of experimental results.

In this study, considering that the experimental modeling was focused on the reliable preproduction of snowdrift on a long-span roof, the similarity number based on the similarity of the drifting snow flux in the saltation layer was selected. These similarity criteria were first introduced by Iversen [17] and also adopted by Delpech [12]. The similitude criterion based on the drifting flux is shown in Equation (1).

$$\left(\rho/\rho_{\mathrm{p}}\right)\left(U^2/2g\right)(1-U_0/U) \tag{1}$$

where ρ and ρ_{p} are the air and particle densities, respectively; U and U_0 are the reference wind velocity and threshold reference velocity, respectively; and g is the gravitational acceleration. Furthermore, similarity criteria related to geometric, dynamic, and kinetic criteria were also considered.

To validate the similarity criterion, snowdrift around a surface-mounted cubic model, employed in detailed field measurements carried out by Oikawa et al. [18] in Sapporo, Hokkaido, Japan, was adopted as the analyzed prototype. The snowdrift was observed for only one day by cleaning up the snow around the model following each drifting snow event. The model was 1.0 m on each edge. The averaged wind velocity was approximately 1.7 m/s at a 1.0 m height, and the maximum wind velocity was close to 4.3 m/s (Figure 3). The snow depth at a reference point was 20 cm. The other measurement parameters are summarized in Table 1. The smallest undulation of snowdrift due to the weak wind velocity and the large snowfall make it the most suitable measurement data for validation of the similarity criteria.

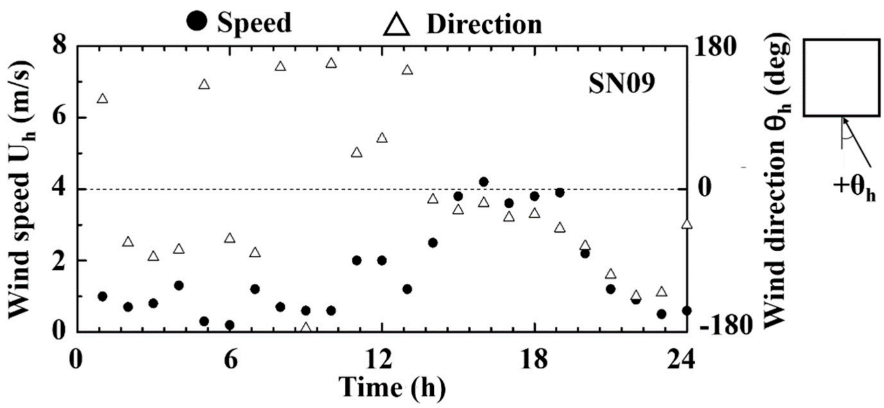

Figure 3. Wind speed U_{h} and direction θ_{h} at 1.0 m height for the entire measuring period on SN09 [18].

Table 1. Prototype drifting parameters.

Particle Parameters	Values	Particle Parameters	Values
Particle diameter D_{p}	150 to 200 µm	Threshold friction velocity U_{t}^{*}	0.15 to 0.36 m/s
Snowfall velocity W_{f}	0.2 to 0.5 m/s	Accumulated snow density ρ_{p}	50 to 700 kg/m^3
Air density ρ	1.22 kg/m^3	Repose angel	30° to 50°

The artificial snow particles were selected for the validation experiment. The air/water ratio in the snowmaker was set to make sure the artificial snow was dry enough to prevent the particles from sticking together. The accumulated snow density was measured with a scale and cylinder; whereas, the particle diameter was measured with a microscope. The snowfall velocity was obtained by measuring the artificial particle falling times from 1.0 m height [8]. The threshold friction velocity was estimated according to an empirical formula [1]. The parameters of the artificial snow particles are summarized in Table 2.

Table 2. Parameters relating to the physical properties of artificial snow.

Particle Parameters	Values	Particle Parameters	Values
Particle diameter D_p	100 to 150 μm	Threshold friction velocity U_t^*	0.3 to 0.6 m/s
Snowfall velocity W_f	2.0 to 2.4 m/s	Accumulated snow density ρ_p	386 to 447 kg/m^3

The selected model scale of 1/2 satisfied the blockage effects. The vertical profiles of the flow field identified over the snow mantle in the test section were similar to these over the measured field in Sapporo. In order to assess the modeling reliability, the results of the typical similarity numbers for both the prototype and model are summarized in Table 3. The experimental wind velocity (2.3 m/s at the height of the model top) used for calculating the scaled model values was determined according to Equation (1). Requirement 2 in Table 3 represents the geometric similarity of both model and prototype. The correct modeling of the ejection process of particles is realized by satisfying requirements 3, 4, and 5. Requirement 5 is a roughness–height Reynold number, where ν is the fluid's kinematic viscosity. The basic requirements of dynamic similarity could be measured with densimetrical Froude numbers 6 and 7 (ratio between the inertia force and gravity force), and similarity number 8.

Table 3. Similitude parameters.

Dimensionless Parameters	Prototype Value	Model Value	Number
D_p/L	1.5×10^{-4} to 2×10^{-4}	2×10^{-4} to 3×10^{-4}	(2)
U/U_t^*	4.7 to 11.3	3.8 to 7.7	(3)
ρ_p/ρ	41 to 574	316 to 366	(4)
$U_t^{*3}/2g\nu > 30$	11.4 to 157	91 to 730	(5)
$\frac{U_t^{*2}}{D_p g}\left(\frac{\rho}{\rho_p - \rho}\right)$	0.02 to 2.21	0.17 to 1.17	(6)
$\frac{U^2}{D_p g}\left(\frac{\rho}{\rho_p - \rho}\right)$	2.58 to 49.38	9.89 to 17.19	(7)
W_f/U	0.1 to 0.3	0.9 to 1.0	(8)

In order to model the fully rough saltation flow, it is desirable to guarantee the lower limit of the Reynolds number $U^{*3}/2g\nu > 30$. If the saltation mechanism occurs, the fully rough flows will be satisfied if $U_t^{*3}/2g\nu > 30$ [16]. This lower limit was satisfied in this experimental case as shown in Table 3. Except for this, the noticeable mismatches are found in the particle ejection process scaling and dynamic similarity. For the particle ejection scaling, the gravitational force is overestimated in requirement 4 with a greater particle density, which is also observed in requirement 8 with a higher snowfall velocity. This indicates that the trajectory of the artificial snow particle is smaller than the natural snow particle one [19]. However, a higher particle/air density ratio is usually required [19] and the saltation trajectory for the scale model is small in comparison with the actual snowdrift observed [20]. For the dynamic similarity, the particulate Froude number weighted by the density ratio (requirement 7) is the parameter that allows for assessing the similarity of the transport mechanism of suspended particles [12]. The evaluation of the particulate Froude number based on the threshold friction velocity (requirement 6) is linked to surface transport. According to comparisons of requirement 6 and requirement 7, the saltation mechanism, which has been identified as the major particle transport process, is better reproduced than other transport processes [12].

The prototype snowstorm duration was assumed to be 24 h according to the observation duration [18]; whereas, the experimental snowstorm duration was set to approximately 8 h according to the definition for the dimensionless time used by Delpech [12]. As the experiment would have been excessively lengthy, the test was divided into four stages to allow the fan to rest and refill the snow particles into the feeder.

2.3. Results and Discussion

Figure 4 compares the dimensionless snow depth distributions obtained from the field measurement and experiment. The snow depths were normalized by the reference snow depth far from the model, which was not affected by the flow around the cube. The deep-colored part in the figure indicates greater snow coverage. The deposition areas in the upwind region ahead of the cube and erosion areas near the upwind corners of the model in the experiment correspond strongly to those of the prototype. However, as the snow particle feeder was set in the upwind region, the air–snow flow originated from the upwind direction. The incoming particles bypassed the model and moved downstream following the separating airflow. Few particles could enter the wake region behind the model with the aid of the vortex. Therefore, the deposition region behind the model was not reproduced in the experiment. Therefore, the building size should be limited to ensure that the entire building was covered by the stable air–snow flow field, on the premise of satisfying the drifting similitude.

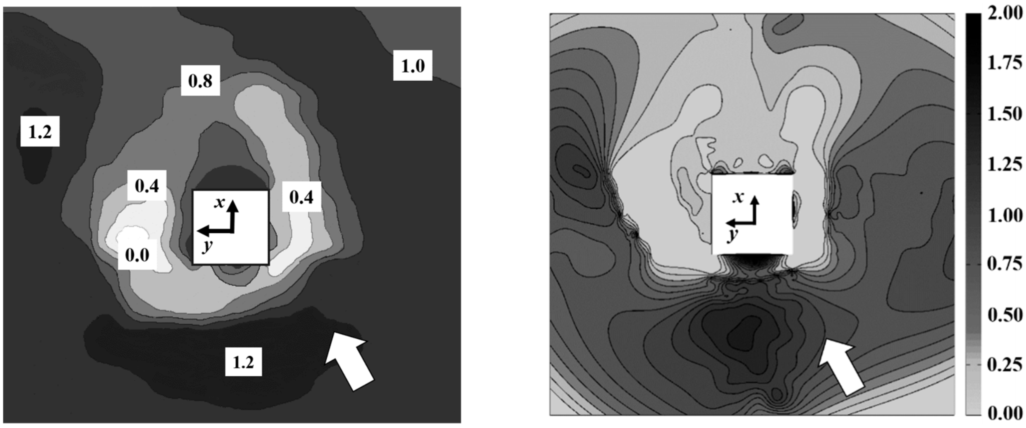

(**a**) (**b**)

Figure 4. Comparison of horizontal distributions of normalized snow depths: (**a**) prototype result [18]; (**b**) experimental result.

3. Experimental Research on Snowdrifts on Complex Long-Span Roof

3.1. Experimental Setup

3.1.1. Test Model

For buildings with a special shape, complex separation and reattachment occur when airflow passes over the roof. The snow load on the roof will be redistributed easily, which may change the stress inside the roof structures, thereby leading to building collapse, especially for long-span lightweight roofs. Therefore, significant attention should be paid to the snow distribution on complex-shaped buildings. Based on the advantages of the experimental method and the validated similarity criterion, a series of snow–wind tunnel tests were conducted to investigate the snowdrift on such complex long-span roofs. In this study, Tongren Olympic Sports Center Stadium was selected as the target building. As the stadium is located on the Yunnan-Guizhou Plateau, China, the frequent snowfall requires additional consideration. The geometric shape of the roof is illustrated in Figure 5a. The cable membrane structure was adopted for the prototype roof. In order to avoid the excessive deformation of the roof, which may affect the safety of the structure and comfortableness of the space, the roof deformation should be strictly controlled at the structural design stage. Therefore, the roof deformation under the action of snow load was assumed to be negligible. Furthermore, considering that the unique roof shape substantially affects the shape of the snow cover, acrylonitrile butadiene styrene (ABS) plastic was used for creating the model roof to reproduce the complex shape as far as possible. Similar hard material was also used by Flaga et al. [13] to make the membrane structure models. Perforated plates were adopted for the sidewall, with an air permeability of approximately 40% to realize the simulation of the wall air permeability (Figure 5b). Based on the above conclusion, the model scale of 1/150 was selected with model size limited to 1.81 (x) × 1.69 (y)0.33 × (z) m.

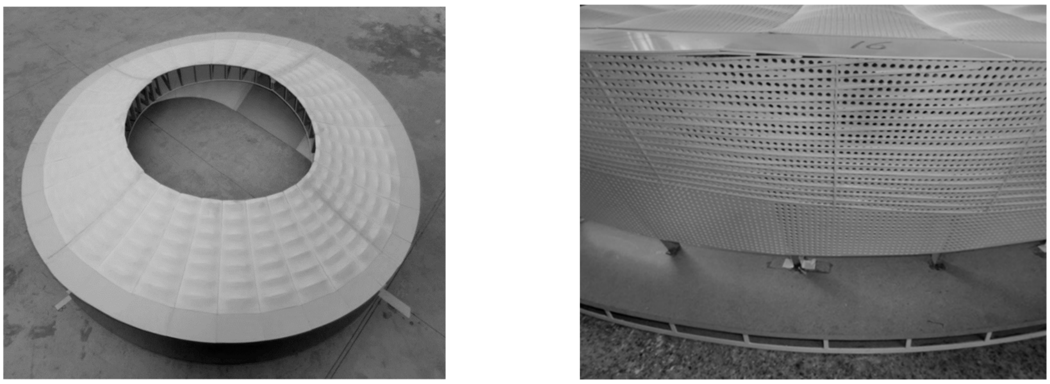

(**a**) (**b**)

Figure 5. Model of membrane structure gymnasium: (**a**) Tongren Olympic Sports Center Stadium model (made of acrylonitrile butadiene styrene (ABS) plastic); (**b**) wall of membrane structure (40% air permeability).

The measuring points were designed according to the special shape of the roof (Figure 6a), combined with the distribution characteristics whereby snow would be deposited in the concave region more easily. Two types of concave regions were formed on the roof: along the radial cable and near the center of each membrane piece. For the concaves along the radial cables, 36 lines were set along the cables, with 16 measuring points set along each line (Figure 6b). For the concaves formed on the membrane, 36 lines were set along the circumferential direction, with an additional 9 measuring points set at the center of each membrane piece (Figure 6b). In total, 900 measuring points were set on the model roof. The snow depth at the measuring point was measured with a snow stick. Furthermore, a snowdrift experiment with an empty field was conducted to simulate the snow distribution on the ground. The shape coefficient μ of the snow distribution on the roof was calculated as the ratio of the snow depth on the model roof to the snow height on the ground.

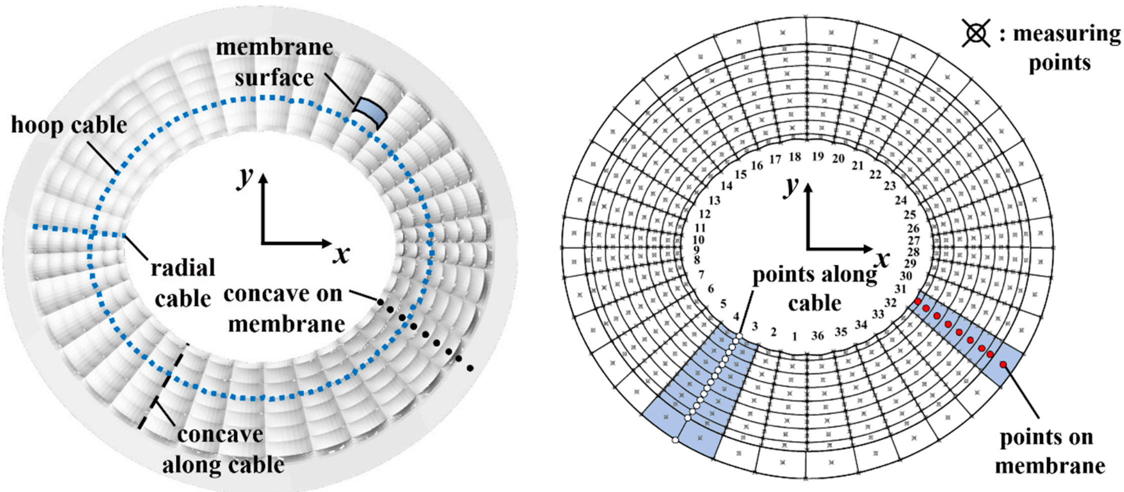

(**a**) (**b**)

Figure 6. Arrangement of measuring points for snow depth: (**a**) roof form; (**b**) arrangement of measuring points.

3.1.2. Setup Parameters

The prototype stadium was constructed in a suburban area of Tongren City, Guizhou province, China. The reference wind pressure is 0.35 kN/m^2 (100 year return period); whereas, the reference snow pressure is 0.35 kN/m^2 (100 year return period) [2]. The prototype wind velocity at a standard height (10 m) during a snowstorm is assumed as 0.45 of the reference wind velocity, calculated based on the reference wind pressure [21]. The air density there is about 1.22 kg/m^3, and hence the reference wind velocity is close to 24 m/s. The snow density is about 150 kg/m^3, and the maximum snow depth during a snowstorm could reach 0.23 m [2]. The threshold friction velocity and snowfall velocity are set to 0.15 m/s and 0.2 m/s, respectively. Regarding the snowfall duration, as no outdoor measuring record was available; the experimental duration was provided based on an eight-year-long outdoor measurement in China by the authors. This work was carried out from 2010 to 2017 and is ongoing. The measurements included the snowfall duration, interval time between two snowfalls, accumulated snow density, and snow depth. Based on the measurement data, a single snowfall usually lasted for nearly 6 to 7 h. The probability of snowfall lasting for less than 12 h was approximately 72% (Figure 7). Therefore, the prototype duration was set as 12 h.

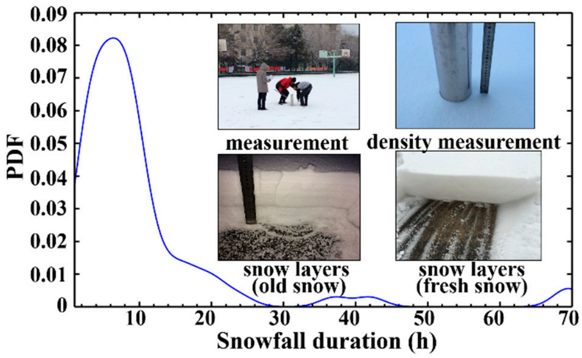

Figure 7. Probability density curve of single snowfall duration, derived from an eight-year field measurement result.

The artificial snow particles were selected as the experimental particles. Prior to the experiment, the snow was sieved into uniform sphere particles. Based on the similarity criterion introduced in Section 2.2, the experiment reference velocity was 1.2 m/s at 0.06 m, and the experimental snowstorm duration was set to 0.6 h. A total of 700 L of artificial snow was poured into the sieve-like feeder during the experimental duration, and the snowfall flux was approximately 0.007 kg/m^{2}s. As this stadium exhibited biaxial symmetry and the wind direction frequency was provided with a 22.5° interval in the annual wind rose diagram, five cases were designed and conducted for different inflow directions at 22.5° intervals, namely 0°, 22.5°, 45°, 67.5°, and 90°, from the x-axis to y-axis (Figure 8).

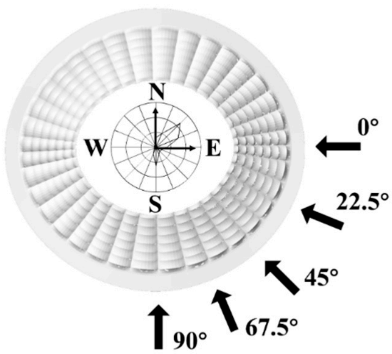

Figure 8. Study cases conducted for different inflow directions at 22.5° intervals (0°, 22.5°, 45°, 67.5°, and 90°).

3.2. Results and Discussion

The snowdrift shape coefficients μ on the membrane roof in different inflow directions are illustrated in Figure 9. The snowdrifts are extremely complex. For different inflow conditions, depositions occur on the windward and leeward surfaces along the air stream. The overall packing forms are approximately fan-shaped. When the inflow direction moved from 0° to 90°, the angle between the windward and leeward depositions varies from 90° to 140°. The results are similar to the unbalanced snow distribution on the umbrella-shaped roof, as indicated in the technical specification for cable structures (Figure 10a) [22]; whereas, in the experimental case, the angle between the depositions changed under asymmetrical conditions because of the non-central symmetrical roof form. Owing to the existence of the concave regions along the radial cables and at the center of each membrane piece, a large amount of snow is accumulated locally and a peak value of approximately 1.8 is generated. This is substantially larger than the peak value of 1.0 for the umbrella-shaped roof, but much closer to the maximum coefficient of the unbalanced distribution on the multi-span gable roof (Figure 10b) [2]. Therefore, the local accumulations that formed on the roof are likely caused by the local form of the roof itself. Evidently, the snow distribution pattern is closely related to the overall and local roof shapes.

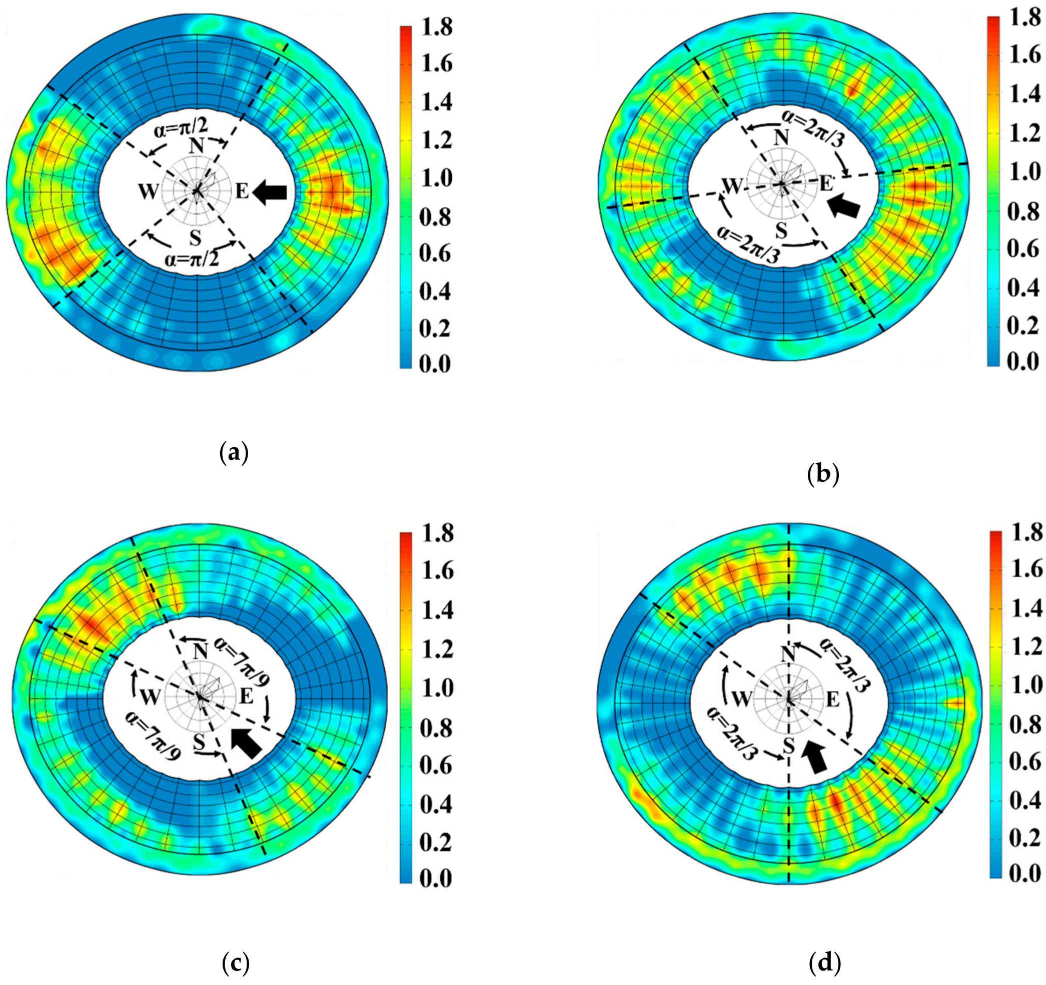

Figure 9. *Cont.*

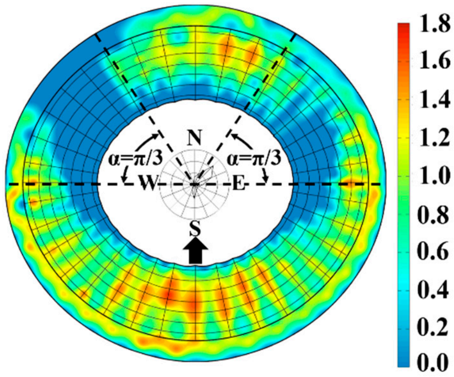

(**e**)

Figure 9. Snow distribution shape coefficient μ: (**a**) 0°; (**b**) 22.5°; (**c**) 45°; (**d**) 67.5°; and (**e**) 90°.

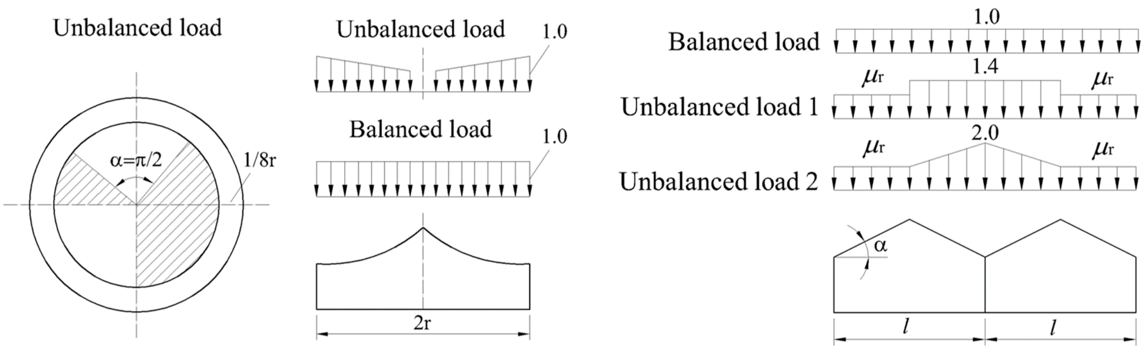

(**a**) (**b**)

Figure 10. Unbalanced distributed shape coefficient on building roofs: (**a**) shape coefficient for umbrella-shaped roof indicated in the technical specification for cable structures; (**b**) shape coefficient for multi-span gable roof indicated in load code for design of building structures.

4. Analysis of Snow Distribution Characteristics

4.1. Analytical Method

To deeply analyze the relationship between the snow distribution pattern and the shape characteristic of the roof, the empirical orthogonal function (EOF) analysis was adopted. This approach is generally used to analyze the structural features in data and extract major data feature quantities. Specifically, EOF analysis can decompose a variable field matrix **X** that changes with time into a time-independent spatial matrix **EOF** and a time matrix **PC**, as shown in Equation (9). In this study, the time-dependent field matrix was replaced by a field matrix that changed with the wind direction, and a wind direction related matrix could be obtained instead of the time matrix. The spatial matrix **EOF** generalizes the geographical distribution characteristics of the field; whereas, the wind direction matrix **PC** is composed of the linear combination of coefficients of the spatial points of the field. As the main information of the original field **X** is concentrated in the first several components of the spatial matrix **EOF**, the study of the original field **X** changing with wind direction can be converted into the investigation of the first components of the spatial matrix **EOF** and their wind direction matrix **PC**, respectively.

$$\mathbf{X} = \mathbf{EOF} \times \mathbf{PC} \tag{9}$$

The specific method is illustrated in Equation (10)–(14). Firstly, a field matrix $\mathbf{X}_{m \times n}$ is obtained by collating the measured data, where the subscript "m" represents the number of spatial points under a certain inflow direction condition, namely 900 and the subscript "n" represents the number of inflow cases, namely five. Based on the orthogonal decomposition theory, the spatial matrix **EOF** and its eigenvalue matrix $\mathbf{\Lambda}$ can be derived, as shown in Equation (11)–(13), where **C** is the cross-product of the field matrix **X** and its transpose matrix $\mathbf{X}^T$. The kth column of the spatial matrix **EOF** represents the kth spatial mode $\mathbf{EOF}_k$. Finally, the wind direction matrix **PC** can be derived from the spatial matrix **EOF** and original field matrix **X**, as indicated in Equation (14).

$$\mathbf{X}_{m\times n} = \begin{bmatrix} x_{11} & x_{12} & \cdots & x_{13} \\ x_{21} & x_{22} & \cdots & x_{23} \\ \cdots & \cdots & \cdots & \cdots \\ x_{m1} & x_{m2} & \cdots & x_{mn} \end{bmatrix} \tag{10}$$

$$\mathbf{C}_{m\times n} = \frac{1}{n}\mathbf{X}\times\mathbf{X}^T \tag{11}$$

$$\mathbf{C}_{m\times n}\times\mathbf{EOF}_{m\times m} = \mathbf{EOF}_{m\times m}\times\mathbf{\Lambda}_{m\times m} \tag{12}$$

$$\mathbf{\Lambda}_{m\times m} = \begin{bmatrix} \lambda_1 & 0 & \cdots & 0 \\ 0 & \lambda_2 & \cdots & 0 \\ \cdots & \cdots & \cdots & \cdots \\ 0 & 0 & \cdots & \lambda_m \end{bmatrix} \tag{13}$$

$$\mathbf{PC}_{m\times n} = \mathbf{EOF}^T_{m\times m}\times\mathbf{X}_{m\times n} \tag{14}$$

4.2. Spatial Matrix Empirical Orthogonal Function (EOF)

According to the EOF theory, each spatial mode EOF_k corresponds to an eigenvalue λ_k. The contribution of EOF_k to the total variance is determined by its eigenvalue λ_k; therefore, the significance of EOF_k can be defined by its eigenvalue. The larger the eigenvalue is, the more significant its influence is. Furthermore, if the eigenvalue error ranges ($\lambda_k - \Delta\lambda$, $\lambda_k + \Delta\lambda$) between two modes overlap, the mode characteristics will be similar. Here, $\Delta\lambda_k$ is determined according to Equation (15), where N^* represents the effective degrees of freedom of data.

$$\Delta\lambda_k = \lambda_k\sqrt{\frac{2}{N^*}} \tag{15}$$

Figure 11 illustrates the eigenvalues of the first few spatial modes. The first three spatial modes (EOF_1, EOF_2, and EOF_3) contribute the most to the total variance; therefore, only the characteristics of these three spatial modes are analyzed in the following. Compared with λ_2 and λ_3, the λ_1 value for EOF_1 leaps significantly. Evidently, EOF_1 has an overwhelming influence on the snow distribution on the stadium roof. The eigenvalues for EOF_2 and EOF_3 are similar, but the significance of EOF_2 is slightly more pronounced. Furthermore, a relatively large overlap exists in the error ranges between EOF_2 and EOF_3, indicating that their distribution patterns are similar.

The distribution characteristic of EOF_1 is illustrated in Figure 12. The values of EOF_1 are all positive. The distribution pattern is indicated by the strip of local accumulations formed in the concave regions along the radial cables, similar to the unbalanced snowpack formed in the eave region between multi-span gable roofs (Figure 10b). In general, EOF_1 further reflects the influence of the local roof shape on the snow load distribution on the building roof. The distribution characteristics of EOF_2 and EOF_3 are illustrated in Figure 13. The spatial characteristics of EOF_2 and EOF_3 are similar, as discussed previously; that is, the overall surface accumulations along the symmetry axes (0° or 90° inflow direction) and skew surface accumulations between the axes (45° inflow direction). These patterns are similar to the fan-shaped depositions on the umbrella-shaped roof (Figure 10a), reflecting the influence of the overall roof shape on the snow load distribution. Moreover, the magnitude of the shape coefficients for EOF_2 and EOF_3 are positive or negative in two perpendicular regions, taking on an opposite distribution pattern with a different inflow direction (the black or gray arrow in Figure 13).

Therefore, EOF_2 and EOF_3 comprehensively reflect the influences of the inflow direction and overall roof shape on the snow load distribution.

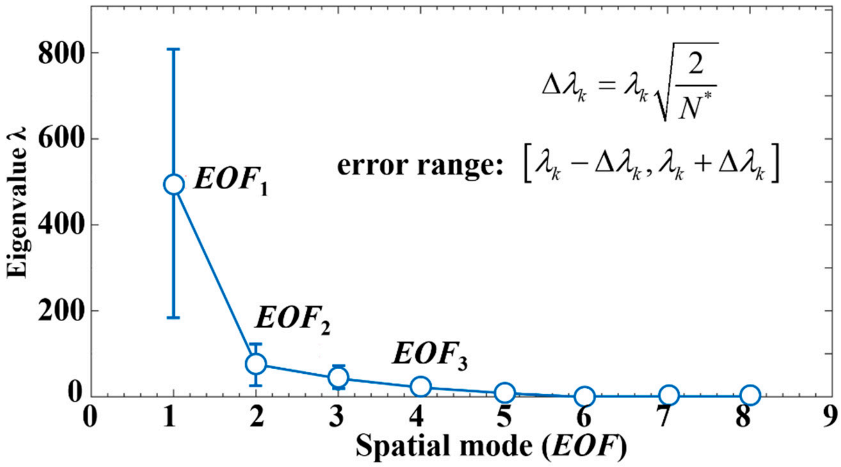

Figure 11. Eigenvalues of each empirical orthogonal function (*EOF*) mode at 95% confidence level.

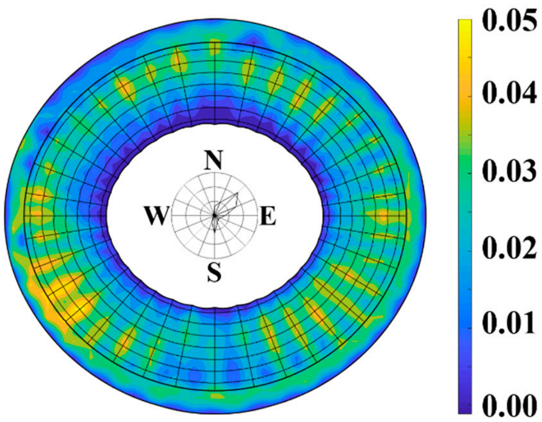

Figure 12. Distribution characteristics of the first spatial mode EOF_1.

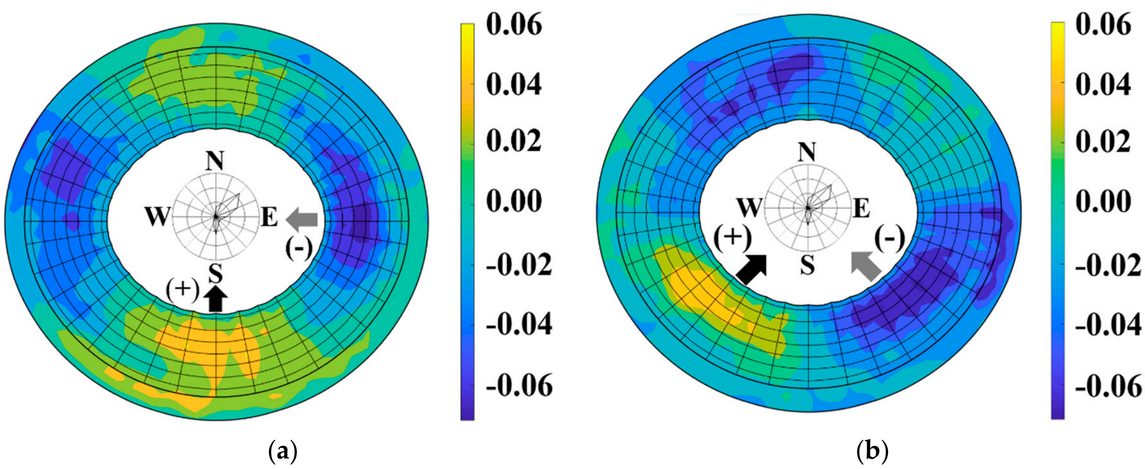

Figure 13. Distribution characteristics of the second and third spatial modes: (**a**) EOF_2; (**b**) EOF_3.

4.3. Wind Direction Matrix ***PC***

As a group of the wind direction-dependent weighted coefficients for the spatial mode, the **PC** coefficient reflects the influence degree and the combination way of the spatial modes. The specific

PC coefficients for EOF_1, EOF_2, and EOF_3 are illustrated in Figure 14. Under the five inflow direction conditions, which range from 0° to 90°, the proportion of the **PC** coefficients for EOF_1 is the largest, indicating an overwhelming influence, as described earlier. The value fluctuates slightly depending on the wind direction and basically remains at 22.5. For EOF_2 and EOF_3, the **PC** coefficients vary sharply with the wind direction, that is, the **PC** coefficients are sensitive to the wind direction. Although the coefficients fluctuate dramatically, the curves of **PC** coefficients are symmetrical along the $PC = 0$ axis with varying inflow directions. Specifically, when the inflow originates from the 0° direction, the inflow direction is consistent with that of the negative state of EOF_2 (gray inflow direction in Figure 13a). The overall snow distribution reflects the characteristics of EOF_2, while the **PC** coefficient for EOF_3 is close to zero. When the inflow originates from the 45° direction, the inflow direction is consistent with that of the negative state of EOF_3 (gray inflow direction in Figure 13b). The overall snow distribution reflects the characteristics of EOF_3, while the **PC** coefficient for EOF_2 is close to zero. Finally, when the inflow moves to 90°, the overall distribution characteristics can be explained only by EOF_2; whereas, the influence of EOF_3 could be neglected. Overall, the local roof shape has the greatest influence on the snowdrift on the complex roof; whereas, the contribution of the whole roof shape to the snowdrift depends on the dominant wind direction. The closer the wind direction represented by the spatial mode is to the dominant wind direction, the greater its contribution to the overall result.

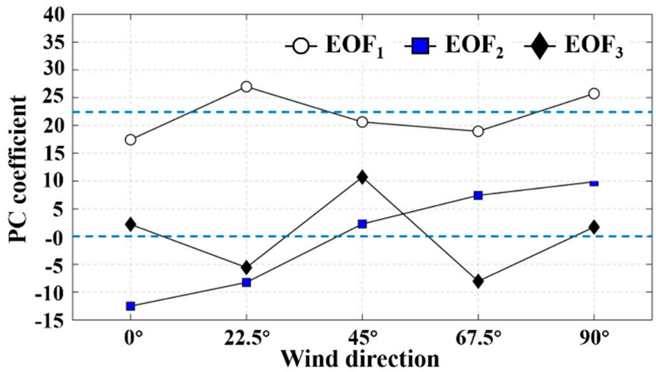

Figure 14. Wind direction coefficients for EOF_1, EOF_2, and EOF_3.

4.4. *Combination of* **EOF** *and* **PC**

Since the original field matrix **X** can be decomposed into a spatial matrix **EOF** and a wind direction matrix **PC**, conversely it is possible to generate the snow distribution on this complex membrane roof through the combination of the spatial matrix **EOF** and wind direction matrix **PC**. As the first three spatial modes made the greatest contribution to the snow distribution on this structure and reflected the influences of the local and overall roof shapes, respectively, the three modes were selected for combination. The combination method is shown in Equation (16). Each column of the generated matrix $\mathbf{X}'$ represents the snow distribution under a specific wind direction condition.

$$\mathbf{X}'_{m\times n} = \mathbf{EOF}_{m\times 3} \times \mathbf{PC}_{3\times n} \tag{16}$$

The generated snowdrifts in different inflow directions are shown in Figure 15. Through comparison with the experimental results as shown in Figure 9, the snowdrift patterns, i.e., the overall fan-shaped deposition occurring on the windward and leeward surfaces along the air stream and the local packing formed in the concave regions along the radial cables and at the center of each membrane piece, show good correspondence with the experimental results. However, it should be noted that a significant underestimation of the shape coefficient values, especially the peak values, is observed. This underestimation was mainly caused by the fact that only the first three modes participated in the combination, and the contribution of the latter modes to the snow distribution was not considered yet. In general, it is preliminarily verified that the snowdrift on a complex roof can be restored by the combination of snow distributions on several corresponding simple roofs.

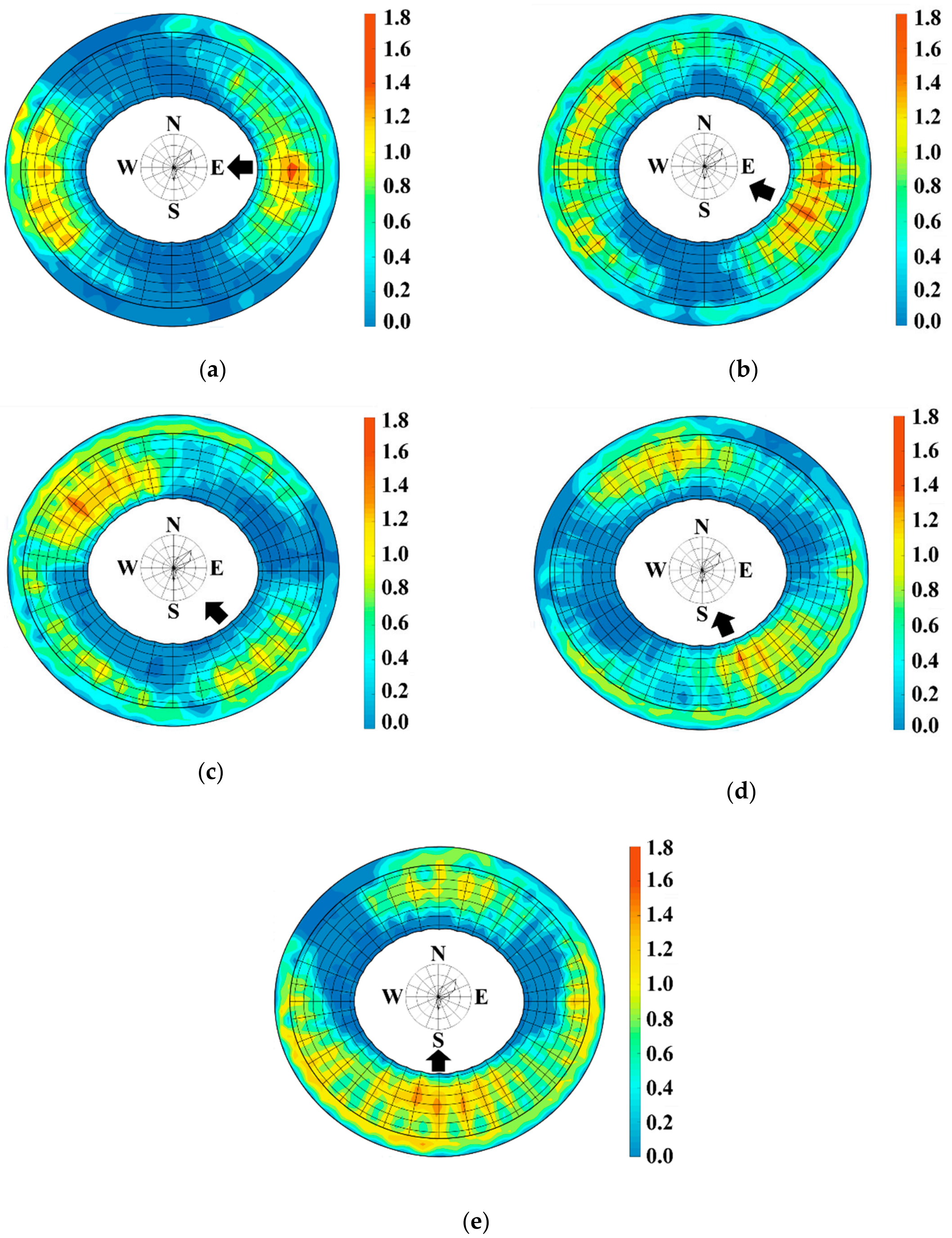

Figure 15. Generated snow distribution shape coefficient μ: (**a**) 0°; (**b**) 22.5°; (**c**) 45°; (**d**) 67.5°; and (**e**) 90°.

In comparison with the conventional methods, the existing national load codes only provide the snow load requirements for simple roofs, as mentioned in Section 1. The applications of the CFD and experimental methods in the prediction of snow loads on complex roofs are also limited, due to the characteristics of time and money consumption. However, this study provides a simplified idea of estimating the snow load on a complex roof. Specifically, in the structural design stage, it is possible for the snow load on a complex roof to be estimated preliminarily by the combination of the snow distributions on several simple roofs, which have been provided in the load code (e.g., dome, curved roof, pitch roof, and obstacle, among others) or can be obtained by numerical studies. This will save a lot of time and money. Unfortunately, as an initial exploration, there are still many problems to be solved. Firstly, the correct selection of simple roofs plays a decisive role in determining the accuracy of combinational results, therefore, the selection method of the corresponding simple roofs should be studied emphatically; secondly, the **PC** coefficients are closely related to roof forms, and a large number of in-depth and large-scale studies should be carried out to clarify the **PC** coefficient; finally, reliable measurement data of snowdrifts on actual complex roofs is indispensable for examining prediction results. However, there is no measurement data available now, due to a large number of works and high risks in the process of measurement. These problems should be considered in future investigations.

5. Conclusions

This study has demonstrated the feasibility of snowdrift reproduction based on the air–snow–wind combined experimental system and the experimental approach. A series of scaled tests were carried out to predict the wind–snow flow behavior on a complex membrane roof. The snow distribution characteristics were decomposed and analyzed, and the following results were obtained. (**i**) The similarity criterion based on the drifting snow flux in the saltation layer was proved to simulate the overall snow distribution effectively. Based on the validated similarity criterion, the snowdrift distributions on a complex long-span membrane roof under different inflow directions were reproduced by using artificial snow particles. The results preliminarily explained the influence of the roof shape and wind direction on the snowdrift, and illustrated the complexity of the snow distribution on the complex roof, compared with that on a simple roof. (**ii**) Based on the EOF analysis, the snow distribution on the complex roof under different inflow direction conditions was broken down into several spatial distribution modes and wind direction-dependent weighted coefficients. Through the analysis of spatial modes, it was proven that the snow load distribution on a complex roof can be broken down into an integral surface load and local concentrated load. Combined with the roof pattern, it was demonstrated that the snow distribution on a complex roof can be decomposed into the snow distributions on several simple roofs according to the specific roof form. (**iii**) Through the significance analysis of the main spatial modes, it was demonstrated that the local roof shape has the greatest influence on the snowdrift on the complex roof; whereas, the contribution of the whole roof shape to the snowdrift depends on the dominant wind direction. The closer the wind direction represented by the spatial mode is to the dominant wind direction, the greater its contribution to the overall result. In practice, when no reference is available in the load code, the actual roof snow load can be estimated preliminarily by reasonable combinations of the existing simple roof snow loads in the codes, referring to the specific roof form and the dominant wind direction.

Author Contributions: Conceptualization, F.F. and S.S.; methodology, G.Z.; software, G.Z.; validation, G.Z., Q.Z., and F.F.; formal analysis, G.Z.; investigation, G.Z.; resources, F.F.; data curation, Q.Z.; writing—original draft preparation, G.Z.; writing—review and editing, G.Z.; visualization, Q.Z.; supervision, F.F.; project administration, S.S.; funding acquisition, F.F.

Funding: This was funded by the Chinese National Natural Science Foundation project (51927813, 51978207) and the National Science Fund for Distinguished Young Scholars (51525802).

Acknowledgments: The authors are grateful to the members of the Space Structures Research Center at the Harbin Institute of Technology, for providing invaluable information and advice in this study.

Conflicts of Interest: The authors declare no conflict of interest. The funders had no role in the design of the study; in the collection, analyses, or interpretation of data; in the writing of the manuscript, or in the decision to publish the results.

References

1. Zhou, X.Y.; Li, X.F. Simulation of snow drifting on roof surface of terminal building of an airport. *Disaster Adv.* **2010**, *3*, 42–50.
2. MOHURD. *Load Code for the Design of Building Structures (GB 50009-2012)*, 1st ed.; China Architecture & Building Press: Beijing, China, 2012; pp. 26–29.
3. BSI. *Eurocode 1-Actions on Structures-Part. 1-3: General Actions-Snow Loads (BS EN 1991-1-3)*, 2nd ed.; CEN: London, UK, 2003; pp. 16–30.
4. ASCE. *Minimum Design Loads for Buildings and Other Structures (ASCE/SEI 7-10)*, 1st ed.; ASCE: Reston, VA, USA, 2010; pp. 29–33.
5. AIJ. *AIJ Recommendations for Loads on Buildings*, 2nd ed.; AIJ: Tokyo, Japan, 2004; pp. 14–18.
6. Tominaga, Y.; Mochida, A. CFD prediction of flowfield and snowdrift around a building complex in a snowy region. *J. Wind Eng. Ind. Aerodyn.* **1999**, *81*, 273–282. [CrossRef]
7. Kwok, K.C.S.; Kim, D.H.; Smedley, D.J.; Rohde, H.F. Snowdrift around buildings for Antarctic environment. *J. Wind Eng. Ind. Aerodyn.* **1992**, *41*, 2797–2808. [CrossRef]
8. Thiis, T.K.; Ramberg, J.F. Measurements and numerical simulations of development of snow drifts of curved roofs. In Proceedings of the Snow Engineering VI, Whistler, BC, Canada, 21–27 September 2008.
9. Thiis, T.K.; Potac, J.; Ramberg, J.F. 3D numerical simulations and full scale measurements of snow depositions on a curved roof. In Proceedings of the 5th European & African Conference on Wind Engineering, Florence, Italy, 19–23 July 2009.
10. Beyers, M.; Waechter, B. Modeling transient snowdrift development around complex three-dimensional structures. *J. Wind Eng. Ind. Aerodyn.* **1999**, *81*, 273–282. [CrossRef]
11. Isyumov, N.; Mikitiuk, M. Wind Tunnel Model Tests of Snow Drifting on a Two-Level Flat Roof. *J. Wind Eng. Ind. Aerodyn.* **1990**, *36*, 893–904. [CrossRef]
12. Delpech, P.; Palier, P.; Gandemer, J. Snowdrifting simulation around Antarctic buildings. *J. Wind Eng. Ind. Aerodyn.* **1998**, *74*, 567–576. [CrossRef]
13. Flaga, A.; Flaga, L. Wind tunnel tests and analysis of snow load distribution on three different large size stadium roofs. In Proceedings of the 8th International Conference of Snow Engineering, Nantes, France, 14–17 June 2016; pp. 232–239.
14. Liu, M.; Zhang, Q.; Fan, F.; Shen, S. Experiments on natural snow distribution around simplified building models based on open air snow-wind combined experimental facility. *J. Wind Eng. Ind. Aerodyn.* **2018**, *173*, 1–13. [CrossRef]
15. Kimura, T. Measurements of drifting snow particles. *J. Geogr.* **1991**, *100*, 250–263. [CrossRef]
16. Kind, R.J. A critical examination of the requirements for model simulation of wind-induced erosion/deposition phenomena such as snow drifting. *Atmos. Environ.* **1976**, *10*, 219–227. [CrossRef]
17. Iversen, J.D. Drifting snow similitude. *J. Hydraul. Div.* **1979**, *105*, 737–753.
18. Oikawa, S.; Tomabechi, T.; Ishihara, T. One-day Observations of Snowdrift around a Model Cube. *J. Snow Eng. Jpn.* **1999**, *15*, 3–13. [CrossRef]
19. Kind, R.J. Snowdrifting: A review of modelling methods. *Cold Reg. Sci. Technol.* **1986**, *12*, 217–228. [CrossRef]
20. Beyers, J.H.M.; Harms, T.M. Outdoor modelling of snowdrift at SANAE IV Research Station, Antarctica. *J. Wind Eng. Ind. Aerodyn.* **2003**, *91*, 551–569. [CrossRef]
21. Mo, H.; Fan, F.; Hong, H. Evaluation of input wind speed used in wind tunnel test and numerical simulation to estimate drifting snow profile. *J. Build. Struct.* **2015**, *36*, 75–90.
22. MOHURD. *Technical Specification for Cable Structures (JGJ 257-2012)*, 1st ed.; China Architecture & Building Press: Beijing, China, 2012; pp. 37–38.